frontiers in Energy Research

ORIGINAL RESEARCH
published: 30 November 2021
doi: 10.3389/fenrg.2021.765612

Polyacrylonitrile/Crown Ether Composite Nanofibres With High Efficiency for Adsorbing Li(I): Experiments and Theoretical Calculations

Tao Ding[1], Qian Wu[2], Mianping Zheng[2], Zhen Nie[2]*, Min Li[3], Suping Peng[1], Yunsheng Wang[2], Xudong Yu[4], Cheng Qian[2], Si Tang[3] and Mingliang Wang[2]*

[1]College of Geoscience and Surveying Engineering, China University of Mining and Technology (Beijing), Beijing, China, [2]MNR Key Laboratory of Saline Lake Resources and Environments, Institute of Mineral Resources, Chinese Academy of Geological Sciences, Beijing, China, [3]School of Chemistry and Chemical Engineering, Chongqing University of Science and Technology, Chongqing, China, [4]College of Materials and Chemistry & Chemical Engineering, Chengdu University of Technology, Chengdu, China

OPEN ACCESS

Edited by:
Yulong Ding,
University of Birmingham,
United Kingdom

Reviewed by:
Jie Lin,
University College London,
United Kingdom
Satyapaul Singh,
Birla Institute of Technology and Science, India

***Correspondence:**
Qian Wu
wuqian0516@163.com
Zhen Nie
nieezhen518@163.com

Specialty section:
This article was submitted to Process and Energy Systems Engineering, a section of the journal Frontiers in Energy Research

Received: *27 August 2021*
Accepted: *12 November 2021*
Published: *30 November 2021*

Citation:
Ding T, Wu Q, Zheng M, Nie Z, Li M, Peng S, Wang Y, Yu X, Qian C, Tang S and Wang M (2021) Polyacrylonitrile/Crown Ether Composite Nanofibres With High Efficiency for Adsorbing Li(I): Experiments and Theoretical Calculations. Front. Energy Res. 9:765612. doi: 10.3389/fenrg.2021.765612

Lithium, as the lightest alkali metal, is widely used in military and new energy applications. With the rapid growth in demand for lithium resources, it has become necessary to improve the effectiveness of extraction thereof. By using chemical grafting and electrospinning techniques, nanofibres containing crown ether were developed for adsorbing Li(I) from the brine in salt lakes, so as to selectively adsorb Li(I) on the premise of retaining specific vacancies of epoxy groups in crown ether. In lithium-containing solution, the adsorbing materials can reach adsorption equilibrium within three hours, and the maximum adsorption capacity is 4.8 mg g^{-1}. The adsorption mechanisms of the adsorbing materials for Li(I) were revealed by combining Fourier transform infrared spectroscopy (FT-IR), scanning electron microscopy (SEM), and X-ray photoelectron spectroscopy (XPS) with density functional theory (DFT) calculation. The results indicated that in crown ether, O in epoxy groups was coordinated with Li(I) to form Li–O and four O atoms in the epoxy groups were used as electron donors. After coordination, two O atoms protruded from the plane and formed a tetrahedral structure with Li(I), realising the specific capture of Li(I). By desorbing fibres that adsorbed Li(I) with 0.5-M HCl, the adsorption capacity only decreased by 10.4% after five cycles, proving ability to regenerate such materials. The nanofibres containing crown ether synthesised by chemical grafting and electrospinning have the potential to be used in extracting lithium resources from the brine in salt lakes.

Keywords: lithium, adsorbing, DFT, selectivity, regeneration

INTRODUCTION

Lithium, as the metal with the lowest density, and has been used in aerospace (Clara and Martins, 2020), medical (Wu and Huang, 2006), and battery (Lee et al., 2018; Wu et al., 2019; Zhang et al., 2019) applications due to its unique physico-chemical properties (Tarascon, 2010). Given the rapid development of portable electronic products and new-energy vehicles, the price of, and demand for, lithium resources have increased sharply in recent years (Xu et al., 2020). According to a United States Geological Survey (USGS) report, 62% of lithium resources in the world are

present in brine in salt lakes (Yu et al., 2019). Therefore, it is of economic and strategic significance to extract lithium resources from the brine in salt lakes.

At present, many researchers have reported the recovery of lithium resources from the brine in salt lakes using methods, such as extraction (Torrejos et al., 2016; Shi et al., 2017; Romero et al., 2020), salinity gradient solar ponds (Nie et al., 2011), and adsorption methods (Hong et al., 2018; Bajestani et al., 2019). Due to advantages such as a simple production process (Meshram et al., 2014), low production cost, and low energy consumption (Xu et al., 2016), the adsorption method has attracted increasing attention in the separation and recovery of lithium resources from the brine in salt lakes. Some researchers have synthesised a manganese (Mg)-based adsorbent with spinel structures ($H_{1.6}Mn_{1.6}O_4$, HMn_2O_4, and $H_4Mn_5O_{12}$) (Feng et al., 1993; Robinson et al., 2010; Xiao et al., 2015; Gao et al., 2018; Liu et al., 2020; Qiu et al., 2021), whose maximum adsorption capacity is reported to have reached 40 mg/g; because of specific selectivity of spinel structures for Li(I), metal ions including Li(I), Mg(II), Ca(II), K (I), and Na(I) in the brine in salt lakes are ranked in descending order according to their distribution coefficient K_d. Such structures can selectively separate and recover lithium resources from the brine in salt lakes. By using polyvinyl chloride (PVC) as a binder and N-methyl pyrrolidone (NMP) as a solvent, Xiao et al. (2015) synthesised granular PVC-$H_4Mn_5O_{12}$ composites with a diameter of 2–3.5 mm through use of the anti-solvent method. Li(I) diffuses internally in the adsorbent, and the mass transfer coefficient is K_f = (1.8–2.5) × 10^{-5} m/s. Chitraka et al. (2001) used the sol–gel method to synthesise layered H_2TiO_3, which is the first ionic sieve type adsorbent adsorbing Li(I) under acidic solution at a pH of 6.5, resulting in an adsorption capacity of 32.6 mg/g. To increase the specific surface area of the adsorbent, some researchers made H_2TiO_3 into nano-tubes by hydrothermal method (Moazeni et al., 2015). The adsorption capacity increases by 5–10%, and the maximum adsorption capacity reaches 39.43 mg/g. Chen *et al.* synthesised magnetic Fe_3O_4 nanoparticles into layered $LiCl{\cdot}2Al(OH)_3{\cdot}nH_2O$ (Li/Al-LDHs) to improve separation effects and the recovery rate of the adsorbing materials from the brine in salt lakes. Moreover, the layered structures of the adsorbing materials were characterised by the quantitative method, thus proving their stability. Although the adsorption capacity of the synthesised magnetic Li/Al-LDHs decreases from 5.83 to 3.46 mg/g, the recovery rate of the adsorbing materials reaches 97%, which improves the efficiency of recovering lithium resources from salt lakes (Chen et al., 2020). Based on the above reports, researchers have studied the stability, adsorption capacity, and recovery of adsorbents, but these adsorbents are particles or powders, which are difficult to recover and have poor permeability in the adsorption process. In actual production, granular adsorbents can be crushed under extrusion and therefore difficult to recover, becoming a bottleneck restricting the industrial application of the adsorption method. This makes it necessary to develop an adsorbing material with good permeability, a high recovery rate, and easy separation in the later stages of processing.

Fibre-based adsorbing materials are ideal adsorbing materials with the advantages of high porosity, large specific surface area, and good internal pore connectivity. By combining the electrospinning method with *in-situ* polymerisation, Wang et al. (2013) prepared polyacrylonitrile/polypyrrole (PAN/PPy) composite nanofibres with core-shell structures to remove Cr(VI) in aqueous solution. The presence of PPy layers on the surface of PAN nanofibres was confirmed by attenuated total reflection-Fourier transform infrared (ATR–FTIR) spectroscopy and X-ray photoelectron spectroscopy (XPS). The materials have good selectivity for Cr(VI) in water. With the decrease of initial pH of the solution, the adsorption capacity increases. When the initial concentration of Cr(VI) in the solution is 200 mg/L, adsorption equilibrium can be reached in 90 min. Deng et al. (2016) synthesised a novel polyacrylonitrile-based fibre modified with thiosemicarbazide (PANMW–TSC) under microwave irradiation and studied the adsorption of the materials for Cd(II) and Pb(II) in aqueous solution. The adsorption capacities separately reach 165.3 and 186.2 mg/g, indicating that the materials effectively adsorb Cd(II) and Pb(II) in wastewater. Choi et al. (2017) synthesised polyethylenimine (PEI)/polyvinyl chloride (PVC)-crosslinked fibre (PEI/PVC-CF) by utilising PEI and PVC as raw materials. The maximum adsorption capacity of the materials for Pd(II) in acidic solution is 146.03 mg/g and after five adsorption cycles, the adsorption capacity remains unchanged. This indicates that the fibre-based adsorbing materials have stable structures and good application prospects. As far as we know, there are few reports on the selective separation of Li(I) from salt lakes based on fibre-based adsorbing materials. This research intended to synthesise nano-sized adsorbing materials by grafting 2-methylol-12-crown-4 (2M12C4) onto nano-SiO_2 by chemical grafting and electrospinning. Moreover, the materials were used for selective separation of Li(I) from the brine in salt lakes.

In the present study, γ-glycidoxypropyltrimethoxysilane (KH560) was used as a coupling agent and 2MI12C4 was grafted onto nano-SiO_2 to synthesise nano-sized adsorbing materials. Furthermore, the nanoparticles were blended into polyacrylonitrile to prepare nanofibres by electrospinning. The materials are new adsorbent materials with low costs, good hydrodynamic properties, and they can be easily separated from solution. The internal structure, stability, and directional capture mechanisms of the adsorbing materials for Li(I) were revealed based on a series of characterisations, adsorption experiments, and theoretical calculations. The results demonstrate that the materials have the potential to be used in the separation and recovery of lithium resources from the brine in salt lakes.

MATERIALS AND METHODS

Materials and Chemicals

The necessary chemical reagents (analytically pure) were mainly purchased from Sinopharm Chemical Reagent Co., Ltd. and Rhawn Reagent Co., Ltd. Detailed information about the reagents was provided in Supporting Material (**Supplementary**

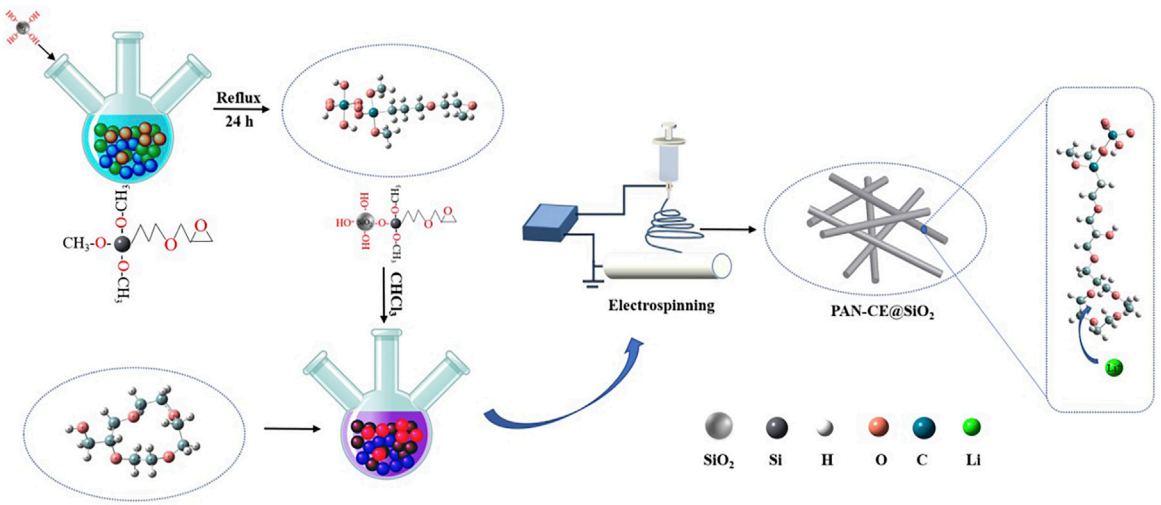

FIGURE 1 | Synthetic route of PAN-CE@SiO_2.

Text S1). The brine was sampled from Zabuye Salt Lake in Tibet Autonomous Region, China and its pH was 8.4. The concentrations of each element were measured by inductively coupled plasma–atomic emission spectroscopy (ICP-AES). The results are summarised in Supporting Material (**Supplementary Table S1**).

Synthesis of 2-Hydroxymethyl-12-crown-4@SiO_2 Nanofibres (PAN-CE@SiO_2)

SiO_2 with a mass of 1 g and KH560 (also 1 g) could be added to a toluene solution (50 ml) for refluxing for 24 h. The solid products were thrice-washed with deionised, then placed in a vacuum oven at 65°C and dried for 12 h. Furthermore, 1 g of the dried solid product, 45 ml trichloromethane ($CHCl_3$), and 1 ml 2M12C4, were simultaneously added to a three-necked flask with a volume of 100 ml and then 2 ml trifluoroacetic acid (CF_3COOH) was added as a catalyst. The solution was stirred for 7 h at a constant temperature of 45°C, thus obtaining CE@SiO_2 after vacuum filtration.

The pre-treated CE@SiO_2 nanopowder (0.5 g) was added to N, N-dimethylformamide for ultrasonic dispersion for 30 min and then PAN fibres were added. The uniform and transparent spinning solution with the concentration of 13 wt% was prepared through magnetic stirring at 90°C for 4 h. The spinning solution was poured into a 10 ml needle syringe with a 18G needle as the spinning head, whose inner diameter was 0.83 mm. After that, the syringe was installed on a micropump for controlling the flow rate of spinning solution. The specific spinning parameters are displayed as follows: the voltage of 15 kV and the flow rate of spinning solution of 0.25 ml/min. Moreover, a drum receiver was rotated at 450 rpm and the receiving distance was 150 mm. The PAN-CE@SiO_2 nanofibres were obtained through vacuum drying of the spinning products in an oven at 45°C for 12 h (**Figure 1**).

Characterisation

The samples in each stage of PAN-CE@SiO_2 synthesis were characterised by utilising techniques, such as scanning electron microscopy (SEM), XPS, and Fourier transform infrared (FT-IR) spectroscopy. The concentrations of ions in the solution were determined by the ICP-AES method. The detailed characterisation information is illustrated in Supporting Material (**Supplementary Text S3**).

Adsorption Experiment

Experiments, such as static adsorption, adsorption selectivity, adsorption kinetics, adsorption isotherms, and cyclic performance were conducted on the adsorbing materials. The data pertaining to the adsorption kinetics were analysed by pseudo-first-order and pseudo-second-order models: data pertaining to the adsorption isotherms were fitted with Langmuir and Freundlich models. Li(I) desorption and recycling performances were studied by using the fixed-bed adsorption method to investigate the ease of regeneration of the adsorbing materials. A series of experiments were conducted on the selective adsorption of the materials for ions from the brine, and the details are shown in Supporting Information (**Supplementary Text S3**).

Calculation Methods

The adsorption mechanisms of PAN-CE@SiO_2 for Li(I) were further calculated based on the density functional theory (DFT): all calculations were conducted by utilising Gaussian 09 software. The B3LYP (Ramos-Sanchez et al., 2013; Zhu et al., 2019) hybrid functional is very reliable in dealing with electron exchange and correlation in a wide range of molecular systems, the initial structure of PAN-CE@SiO_2 and Li(I) composites was optimised by 6–31+G (d, p) basis sets of the B3LYP hybrid functional. In addition, the natural bond orbit (NBO) of the composites was calculated by using 6–31+G (d, p) (Wang et al., 2020) basis sets of the B3LYP hybrid functional, which allowed

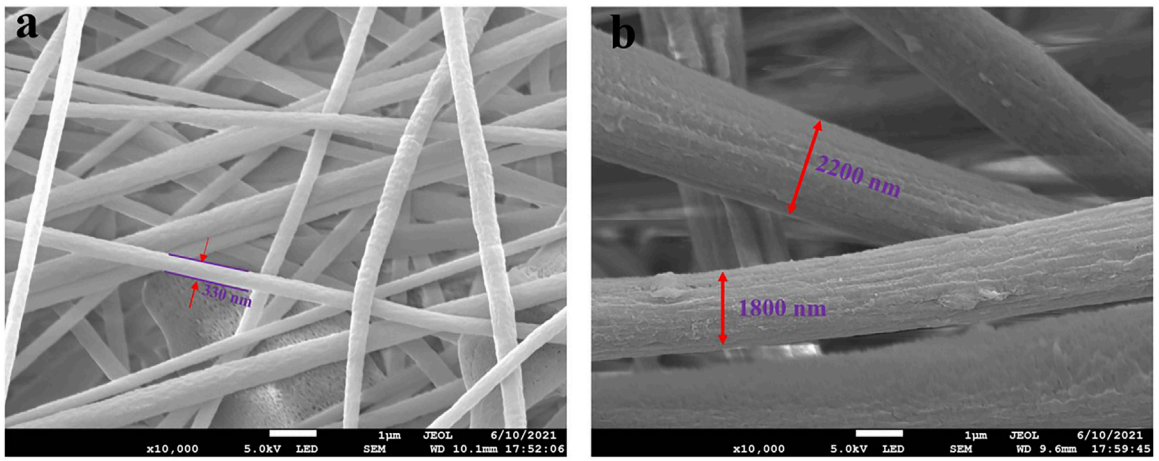

FIGURE 2 | SEM images before **(A)** and after **(B)** the adsorption of PAN-CE@SiO_2 for Li(I).

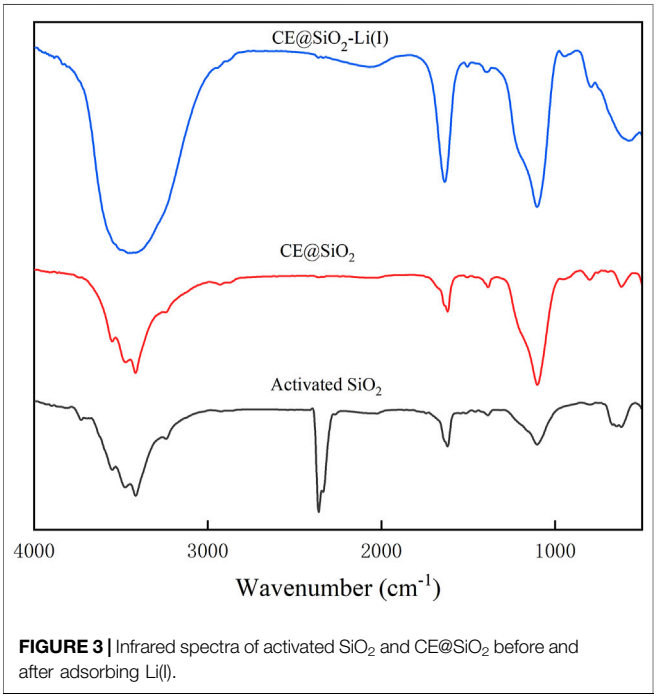

FIGURE 3 | Infrared spectra of activated SiO_2 and CE@SiO_2 before and after adsorbing Li(I).

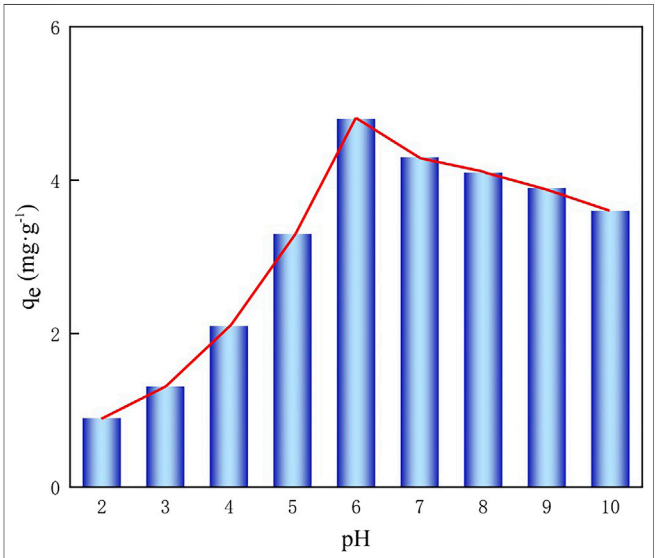

FIGURE 4 | Influences of the pH value on the adsorption capacity of PAN-CE@SiO_2 for Li(I).

further analysis of the mechanisms of interaction between functional groups in PAN-CE@SiO_2 and Li(I). The details are provided in Supporting Information (**Supplementary Text S4**).

RESULTS AND DISCUSSION

Characterisation of PAN-CE@SiO_2

In **Figure 2A**, regular nanofibres have uniformly distributed diameters of about 330 nm and smooth surfaces, and a large number of pores are distributed between fibres, which are conducive to capture (by PAN-CE@SiO_2) of target ions from the brine. Infrared spectra of activated SiO_2 as well as CE@SiO_2 before and after adsorbing Li(I) are displayed in **Figure 3**. In all samples, absorption peaks attributed to–O–, C=C and Si–O stretching vibrations can be observed at 1,140 (Kong et al., 2004), 1,640, and 479 cm^{-1} (Zhong et al., 2021), respectively. After chemical grafting, an absorption peak attributed to the stretching vibration of epoxy groups in 2M12C4 is found at 590 cm^{-1} and the absorption peak assigned to the C–H stretching vibration in 2M12C4 appears at 2,875 cm^{-1}. Moreover, the absorption peak at 3,525 cm^{-1} is assigned to O–H stretching vibration in 2M12C4. The characteristic absorption peak of–O– at 1,140 cm^{-1} is significantly enhanced and becomes wider and sharper (Sileika et al., 2011; Salih et al., 2015),

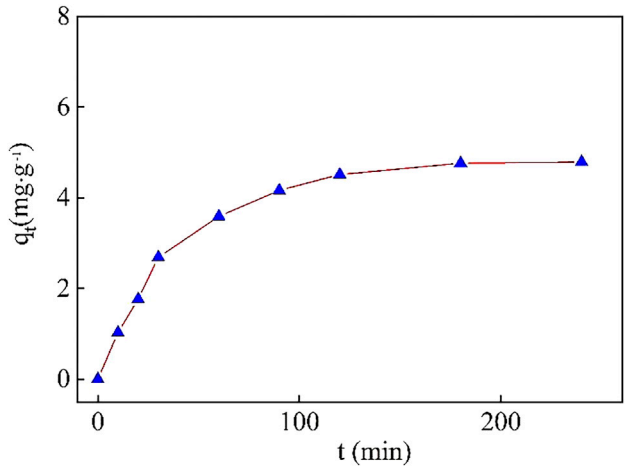

FIGURE 5 | Change in adsorption capacity with time.

suggesting that the chemical reaction used to prepare nanofibres by grafting 2M12C4 onto the activated SiO_2 had succeeded.

Effects of pH on Adsorption

The pH value is an important factor affecting the adsorption for metal ions, because it can change the forms of metal ions in aqueous solution and the number of charges on the surface of the adsorbing materials. As displayed in **Figure 4**, the effects of PAN-CE@SiO_2 with changing pH value in the range of 2–10 on the adsorption capacity for Li(I) were evaluated (because the as-prepared materials can be damaged at other pH values). **Figure 4** demonstrates that the adsorption capacity gradually increases when the pH is increased from 2.0 to 6.0. When the pH value is about 6.0, the adsorption capacity for Li(I) reaches the maximum and is 4.8 mg/g; as the pH value is increased beyond 6.0, the adsorption capacity begins to decrease. The reason for this is as follows: when the pH value is low, there is much free H^+ in the solution and functional groups can be protonated. Moreover, O in epoxy groups binds with H^+, so the number of binding sites on Li(I) decrease. Therefore, the adsorption capacity gradually decreases when the pH value is less than 6.0. As the pH value is increased beyond 6.0, the concentration of OH^- in the solution increases, which may cause some Li(I) in the solution to be present in the form of $[Li(OH)_2]^-$, thus affecting coordination between O–in epoxy groups in PAN-CE@SiO_2 and Li(I). Therefore, the adsorption capacity gradually decreases when the pH value exceeds 6.0.

Adsorption Behaviours

Figure 5 show the changes in adsorption of the adsorbent for Li(I) with time: there is a rapid adsorption of Li(I) by the adsorbent. The adsorption rate for Li(I) exceeds 90% at about 2 h and the whole adsorption process can reach basic equilibrium within 3 h. This may be because rings of epoxy groups in PAN-CE@SiO_2 are opened to form a C–O– structure, which adsorbs Li(I). The decrease of the adsorption rate in the later stage may be due to the reduction of the C–O– structure without coordination with Li(I) and the concentration of free Li(I) in the solution, so that the adsorption rate decreases. In the preparation of the adsorbent, epoxy groups in crown ether are specific vacancies for Li(I) adsorption. These adsorption sites are usually located deeper in the adsorbing materials, and the rings cannot be opened unless eluted with dilute HCl, however, Li(I) is migrated inwards only by molecular diffusion, resulting in a longer time to reach overall adsorption equilibrium.

The better to reveal adsorption mechanisms of PAN-CE@SiO_2 for Li(I), the experimental data were analysed by using two common kinetic models (the pseudo-first-order and pseudo-second-order kinetic models). **Table 1** lists relevant kinetic parameters, while the fitting curve of kinetics is shown in **Supplementary Figure S1**. Based on kinetic data, the pseudo-second-order kinetic model is better suited to describing the whole adsorption process (the correlation coefficient reaches 0.998). The maximum equilibrium adsorption capacity calculated through the pseudo-second-order kinetics is closer to the experimental data, so it can be considered that this is a chemical adsorption process. As expected, it is the presence of epoxy groups in PAN-CE@SiO_2 that provides the C–O– structure, which determines the amount of Li(I) bound thereto. In the preparation of the adsorbent, the vacancies for Li(I) adsorption reside in epoxy groups between PAN-CE@SiO_2 layers and the diffusion of Li(I) between PAN-CE@SiO_2 layers is the dominant factor governing the whole adsorption process. Therefore, through a certain temperature rise or proper stirring, the overall adsorption process can be accelerated.

The adsorption isotherms are illustrated in **Figure 6**: with the increase of the initial concentration, the equilibrium adsorption capacity of the adsorbing materials for Li(I) rises. As the concentration of Li(I) in the system rises, the driving force for mass transfer increases. As mentioned above, the adsorption sites for Li(I) in the prepared adsorbing materials are from epoxy groups in crown ether grafted onto SiO_2 during preparation, so the number of adsorption sites for Li(I) in the adsorbent is fixed. When the adsorption sites in epoxy groups are largely all occupied by Li(I), the adsorption capacity will not change to any significant extent thereafter.

In this study, the experimental data were fitted by Freundlich and Langmuir adsorption isotherm models and the relevant data are listed in **Table 2**. It can be found that the correlation coefficient fitted by the Langmuir adsorption isotherm model is closer to 1 and the calculated maximum adsorption capacity is closer to the measured adsorption capacity, suggesting that the adsorption process is more consistent with the Langmuir adsorption isotherm model and the adsorption process entailed monolayer adsorption. The reason for this is as

TABLE 1 | Kinetic parameters.

Pseudo-first-order			Pseudo-second-order		
k_1 (min^{-1})	$q_{e,\ cal}$ (mg/g)	R_1^2	k_2 (mg/(g·min))	$q_{e,\ cal}$ (mg/g)	R_2^2
0.032	6.9	0.955	0.007	5.1	0.998

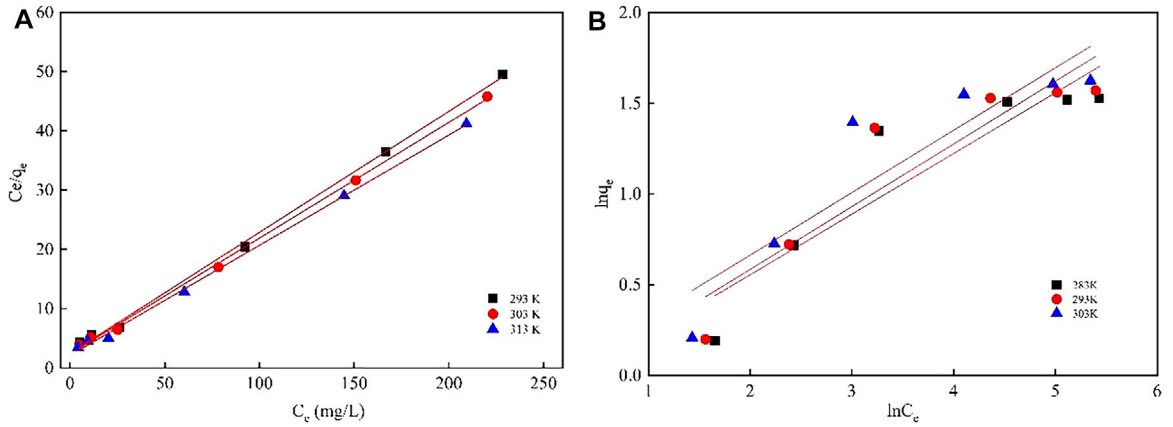

FIGURE 6 | Comparison of Langmuir **(A)** and Freundlich **(B)** adsorption models for the Li(I) adsorption of the adsorbing materials.

TABLE 2 | Relevant parameters of Langmuir and Freundlich models.

Temperature (*K*)	$q_{e,\ exp}$ (mg/g)	Langmuir				Freundlich	
		$q_{m,\ cal}$ (mg/g)	K_L (L/mg)	R^2	*n*	K_f (mg/g)	R^2
283	4.6	4.9	0.082	0.998	2.99	1.121	0.801
293	4.8	5.1	0.084	0.997	2.89	1.113	0.816
303	5.1	5.4	0.088	0.998	2.91	1.025	0.792

TABLE 3 | Adsorption performance of adsorbents for Li(I) in studies.

Adsorbent	Adsorption equilibrium time (h)	Ref.
$Li_4Mn_5O_{12}$	10	Xiao et al. (2015)
Li/Al-LDHs	24	Sun et al. (2019)
Li_2TiO_3	24	Chitrakar et al. (2014)
$Li_{l.6}Mn_{l.6}O_4$	72	Chitrakar et al. (2001)
PAN-CE@SiO_2	3	This study

follows: the number of effective adsorption sites for Li(I) is fixed during preparation of the adsorbent. Moreover, there is a certain space between these vacancies for Li(I) adsorption, while there is no interaction between the vacancies for adsorption. Compared with lithium-adsorbing materials reported in recent studies, the PAN-CE@SiO_2 used in the present study exhibits a faster adsorption rate (**Table 3**) and can reach adsorption equilibrium in 3 h. This suggests that the adsorption sites of PAN-CE@SiO_2 are easier to identify, which imparts excellent adsorption kinetics to the material.

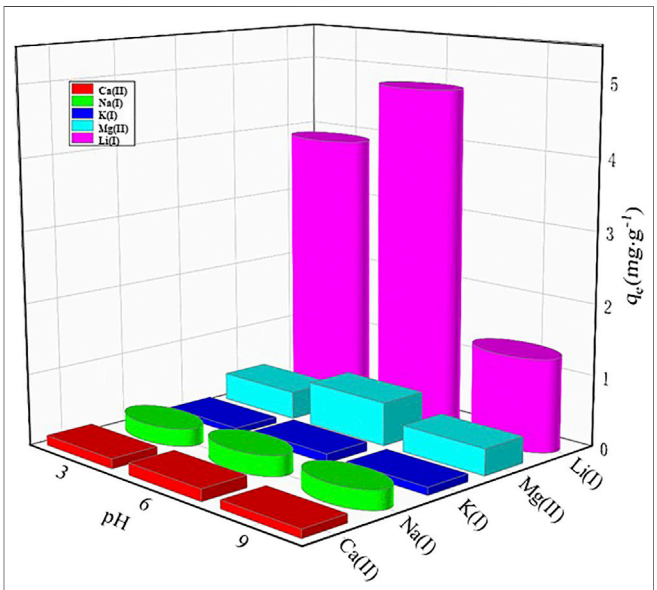

FIGURE 7 | Competitive adsorption under different pH values.

Selectivity and Ability to be Regenerated

The selectivity and ability to be regenerated of the adsorbing materials are important factors determining whether the adsorbing materials can be industrialised or not. Owing to Li(I) being generally associated with Mg(II), Na(I), Ca(II), and K(I) in the brine in a salt lake, these four metal ions were selected to investigate the selectivity of the adsorbing materials for Li(I). **Figure 7** demonstrates the competitive adsorption results of PAN-CE@SiO_2 for ions in solution at pH values of 3, 6, and 9 and **Table 4** lists relevant selectivity parameters. It can be found from **Figure 7** that the adsorption capacity of the adsorbing

TABLE 4 | Adsorption parameters for selectivity of PAN-CE@SiO_2.

ions	pH	Distribution coefficient (K_d) (ml/g)		Selectivity coefficient (*K*)
		D (*Li*)	D (*M*)	
Li(I)/Mg(II)	3	27.33	7.86	3.48
	6	106.44	12.56	8.47
	9	85.54	8.47	10.18
	3	27.13	5.63	4.65
Li(I)/Na(I)	6	106.68	5.83	18.30
	9	84.13	4.82	17.45
	3	26.48	2.20	12.04
Li(I)/K(I)	6	101.81	2.61	39.01
	9	89.32	1.80	49.62
	3	27.54	2.20	12.52
Li(I)/Ca(II)	6	106.68	3.41	31.38
	9	77.59	2.81	27.61

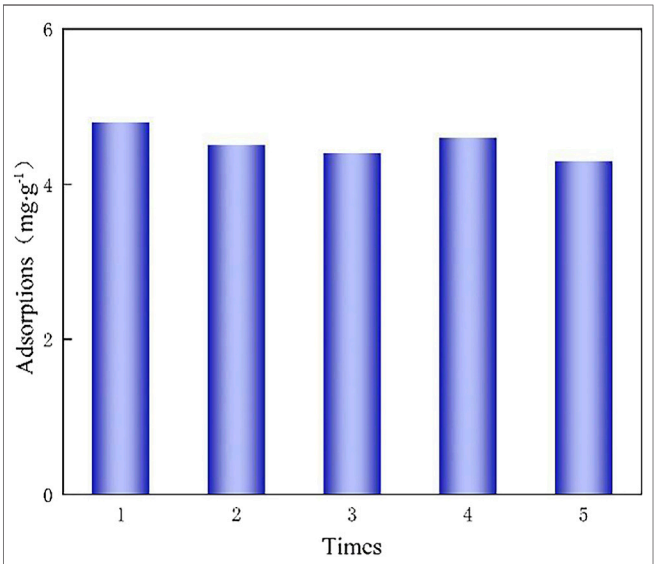

FIGURE 8 | Cyclic capacity.

materials for Li(I) in the mixed solution is much greater than those for the other metal ions and Li(I), Mg(II), Na(I), Ca(II), and K(I) are ranked thus in descending order according to competitive adsorption. When the pH value is 6, the adsorption capacities of each ion are maximised. This may be because free H^+ under acidic conditions at a pH value of 3 can bind with more C–O–, thus reducing the number of effective adsorption sites in epoxy groups. Under alkaline conditions at a pH value of 9, the OH^- concentration in the solution is high and many complex ions are produced, influencing binding between C–O– and metal ions. It is evident that PAN-CE@SiO_2 has a certain affinity to Mg(II), probably because vacancies in epoxy groups of crown ether are matched with the diameter of Li(I), while the radius (0.065 nm) of Mg(II) is close to that (0.068 nm) of Li(I). Therefore, PAN-CE@SiO_2 can adsorb a certain amount of Mg(II).

For PAN-CE@SiO_2 reaching saturated adsorption, Li(I) can be eluted with 0.5-M HCl. After five adsorption-desorption cycles in the solution with the pH value of 6, PAN-CE@SiO_2 still maintains its good adsorption performance and selectivity for Li(I) (**Figure 8**) and the adsorption capacity reaches 4.3 mg/g. The selectivity coefficients for Mg(II), Na(I), K(I), and Ca(II) are 8.47, 18.30, 39.01, and 31.38, respectively. Therefore, the prepared adsorbing materials have good stability and broad application prospects.

Adsorption Mechanisms

The adsorption mechanisms for Li(I) on the surface of PAN-CE@SiO_2 were revealed from a macroscopic perspective through an adsorption experiment. By means of XPS, FT-IR spectroscopy, and theoretical calculation, the capture mechanisms of adsorption sites for Li(I) were further explained from a microscopic perspective. The relevant adsorption mechanisms are shown in **Figure 9**.

Figure 3 compares infrared spectra of the adsorbent before and after adsorbing Li(I). The absorption peak assigned to C–H stretching vibration in 2M12C4 migrates from 2,875 cm^{-1} on the CE@SiO_2 curve to 2,890 cm^{-1} on the CE@SiO_2-Li(I) curve. The absorption peak ascribed to stretching vibration of epoxy groups in 2M12C4 at 590 cm^{-1} on the CE@SiO_2 curve migrates to 770 cm^{-1} on the CE@SiO_2-Li(I) curve. This is probably because more energy is required for vibration of bound metal ions. In addition, several studies show that this is caused by adsorption of N- and O-containing functional groups for metal ions. **Figure 2B** shows an SEM micrograph after adsorption of Li(I): compared with the SEM image before adsorption, the diameter of nanofibres increases and the surface becomes rougher after adsorption. The reason for this may be that the volume of epoxy groups in PAN-CE@SiO_2 increases after adsorption of Li(I) and the introduction of Li(I) makes the surface of the adsorbent rougher. **Figure 10** shows full-spectrum fitting 1) and narrow-spectrum fitting 2) of XPS before and after the adsorption of PAN-CE@SiO_2 for Li(I). On the curve after Li(I) adsorption in **Figure 10A**, in addition to the original elements, an obvious characteristic peak corresponding to the presence of lithium appears at 55.84 eV. The right-shift of the main peak indicates that Li(I) has been coordinated with adsorption sites in PAN-CE@SiO_2. Besides, **Figure 10B** illustrates the peak fitting of C–O before and after the adsorption for Li(I). After the adsorption,

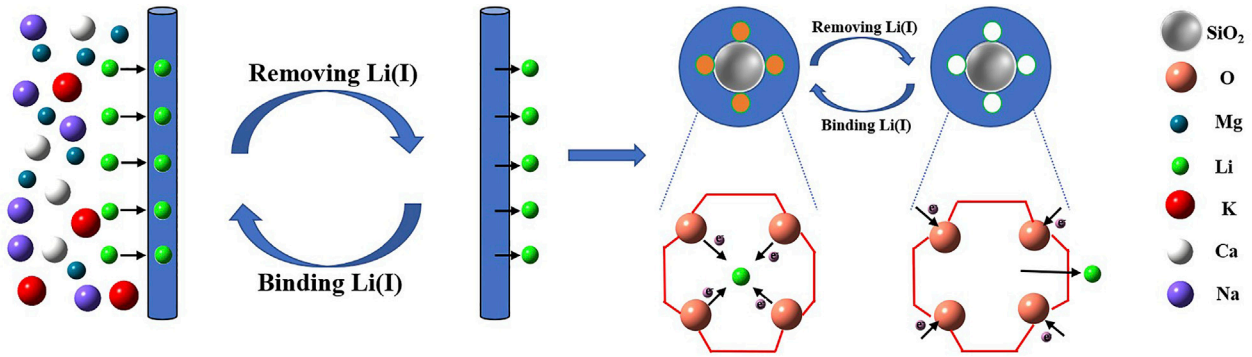

FIGURE 9 | Adsorption mechanisms for Li(I) on the surface of PAN-CE@SiO_2

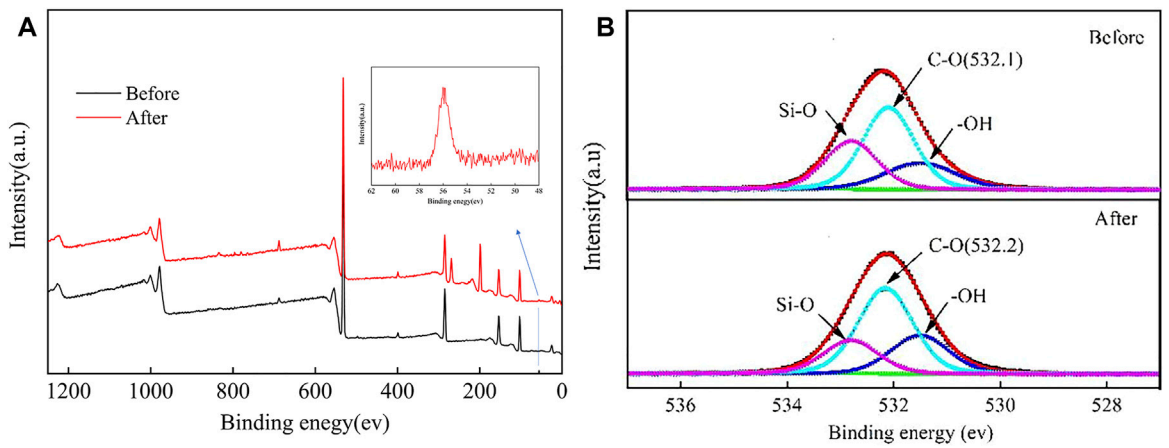

FIGURE 10 | Full-spectrum fitting **(A)** and narrow-spectrum fitting **(B)** of PAN-CE@SiO_2 by XPS.

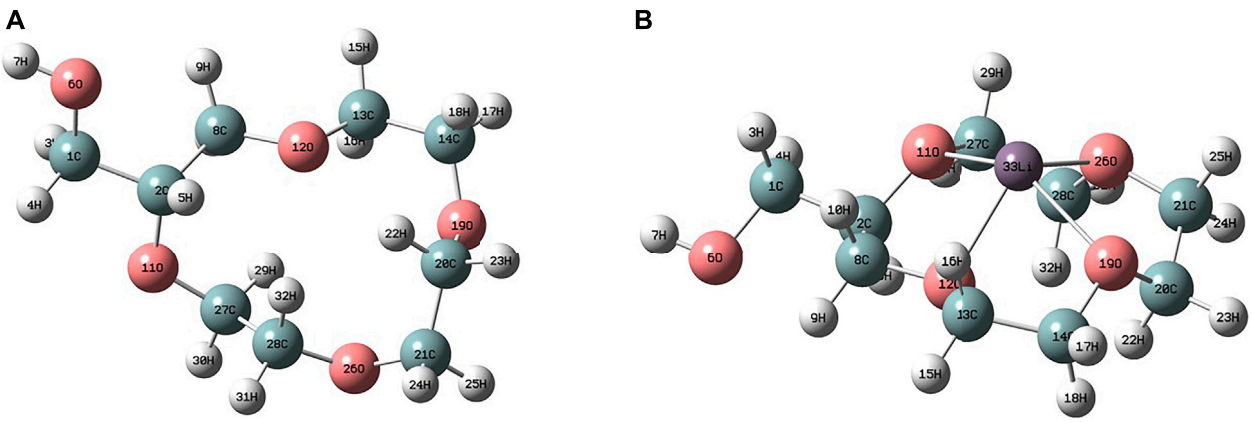

FIGURE 11 | Structural optimisation before **(A)** and after **(B)** the adsorption of PAN-CE@SiO_2 for Li(I).

the characteristic peak of C–O changes from 532.1 to 532.2 eV, probably because the O in C–O (as an electron donor) is involved in the adsorption of Li(I).

The adsorption mechanisms of PAN-CE@SiO_2 for Li(I) were explored by way of DFT calculation. **Figure 11** shows the optimal structures before and after surface functional groups bind with

TABLE 5 | The calculated parameters for the complex.

Complex	Interaction energy (kcal/mol)	NBO partial charge		M(II) electron configuration	*E*(2) energy (kcal/mol)			
		Ligand	M (I)		LP(O10)–LP*(M)	LP(O11)–LP*(M)	LP(O18)–LP*(M)	LP(025)–LP*(M)
Li(I) complex	−232.18	0.245	0.755	$2s^{0.08}3p^{0.16}3d^{0.01}$	14.30	12.04	12.53	14.29

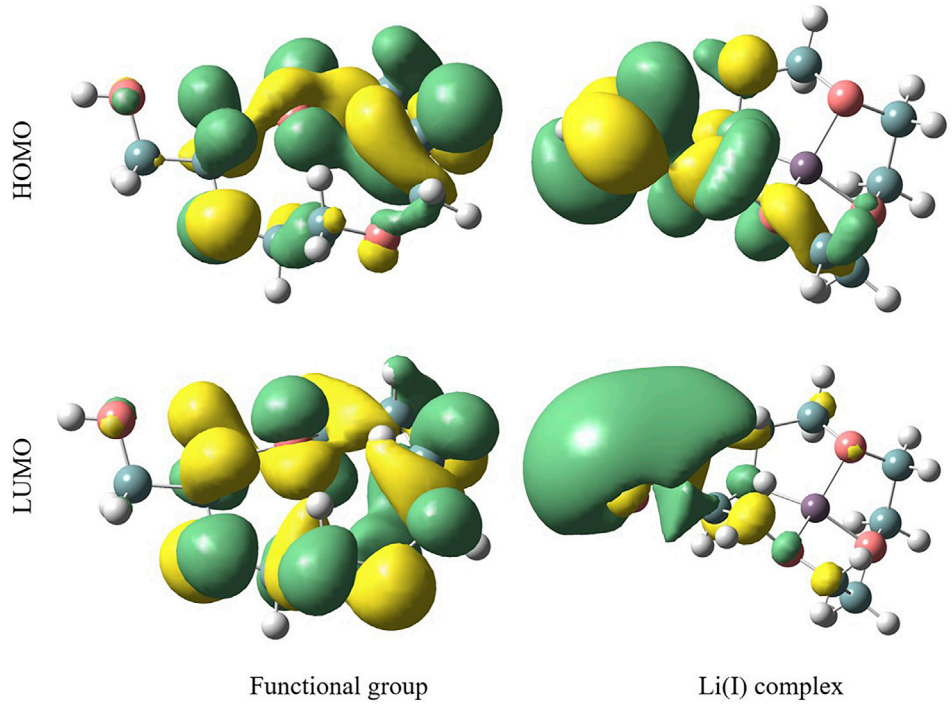

FIGURE 12 | HOMOs and LUMOs before and after the adsorption of PAN-CE@SiO_2 for Li(I).

Li(I) and the relevant calculation parameters are listed in Supporting Information (**Supplementary Table S3**). It is found that four O atoms in functional epoxy groups in 2M12C4 simultaneously bind with Li(I) to form a tetrahedral structure and Li(I) is located above the crown ether ring. As listed in **Table 5**, after coordination with Li(I), and the bond angles of two C–O–C in the functional epoxy groups of 2M12C4 decrease from 118.29 eV (117.15 eV) to 117.25 eV (115.07 eV) in terms of the binding energy, respectively. This is because the minimum cavity size in the complex of 2M12C4 and Li(I) is 3.44 Å, which is much smaller than the sum (4.32 Å) of the ion diameters of Li(I) and O^{2-}. Therefore, during coordination, the vacancies in functional epoxy groups in 2M12C4 cannot hold Li(I), and two O atoms bend out of the plane to bind with Li(I).

Through NBO, the mechanisms of action between functional groups and metal ions were further analysed and salient calculation parameters are listed in **Table 5**. The binding energy of Li(I) complex is −232.18 kcal/mol, indicating a strong affinity of PAN-CE@SiO_2 to Li(I). Furthermore, the analysis of NBO partial charge shows that the charge of Li(I) is 0.755, while that of the ligand is 0.245. This result suggests that there is charge transfer between surface functional groups and metal ions in the process of adsorption. As shown in **Table 5**, the natural layout of electrons of Li(I) is expressed as $2s^{0.08}3p^{0.16}3d^{0.01}$, indicating that electrons are mainly transferred from functional groups to the 3p orbit of Li(I). This is also consistent with the fitting results of XPS in **Figure 11**, that is, C–O– in epoxy groups of PAN-CE@SiO_2 (as an electron donor) is involved in the coordination of Li(I).

Figure 12 compares the highest occupied molecular orbitals (HOMOs) and lowest unoccupied molecular orbitals (LUMOs) before and after the adsorption of PAN-CE@SiO_2 for Li(I). It can be observed from the figure that the HOMOs before the adsorption of PAN-CE@SiO_2 are mainly distributed on epoxy groups of 2M12C4, while they are mainly found on three O atoms and adjacent C and H atoms in epoxy groups of 2M12C4 after the adsorption process. Before the adsorption of PAN-CE@SiO_2, the LUMOs are almost distributed throughout the whole functional group, and after adsorption of Li(I), they are mainly shown on C, H, and O atoms (other than epoxy groups), further evincing the

electron transfer between ligand and metal ions during the adsorption process. Meanwhile, according to second-order Moller-Plesset perturbation theory, the stabilisation energy *E* (2) reflects the degree of delocalisation of electrons. The stabilisation energy *E* (2) of this metal complex was calculated (**Table 2**): the stabilisation energies *E* (2) of LP(O10)–LP*(Li), LP(O11)–LP*(Li), LP(O18)–LP*(Li), and LP(O25)–LP*(Li)) of Li(I) are 14.30, 12.04, 12.53, and 14.29 kcal/mol, respectively. This further verifies that PAN-CE@SiO_2 mainly depends on the electron transfer between the four O atoms in epoxy groups of 2M12C4 and Li(I) to produce coordination and form a stable complex, thus achieving the purpose of adsorption. This also corresponds to XPS and FT-IR results, that is, the four O atoms in epoxy groups (as electron donors) coordinate with Li(I), to adsorb Li(I).

CONCLUSION

A new type of complex nanofibre, namely adsorbing material PAN-CE@SiO_2, was developed by grafting 2M12C4 onto activated SiO_2 and applied to the brine in a salt lake to adsorb Li(I) in a selective manner. A series of characterisation and adsorption experiments on PAN-CE@SiO_2 were conducted. The results show that the selectivity coefficients of PAN-CE@SiO_2 for Mg(II), Na(I), K(I), and Ca(II) in the mixed solution with the pH value of 6 are, separately, 8.47, 18.30, 39.00, and 31.38, proving that PAN-CE@SiO_2 can selectively adsorb Li(I). When the pH value is 6, the adsorption capacity is maximised at 4.8 mg/g. The adsorption kinetics confirms to the pseudo-second-order model, while the isothermal adsorption model is in line with the Langmuir model. The adsorption process is one of chemical adsorption. The directional selective adsorption mechanisms of the adsorbing materials for Li(I) were revealed by combining FT-IR, SEM, and XPS with DFT calculation. After five cyclic adsorption-desorption experiments, the adsorption capacity remains at 4.3 mg/g, indicating that PAN-CE@SiO_2 has good stability and can be regenerated. PAN-CE@SiO_2 can be used to separate and recover lithium resources from the brine in a salt-lake, so making it a promising new adsorbing material with the potential for industrial application.

DATA AVAILABILITY STATEMENT

The original contributions presented in the study are included in the article/**Supplementary Material**, further inquiries can be directed to the corresponding authors.

AUTHOR CONTRIBUTIONS

TD, major write up and review; QW and ZN, conception, outline, major write up, and review; ML, SP, YW, XY, MW, CQ, and ST, critical review, content suggestions, and proofreading; MZ, critical review, content suggestions, and proofreading.

FUNDING

This work is partially supported by the Process and Mechanism of Resource Element Loss in Typical Salt Lake System of Qaidam (U20A20148).

SUPPLEMENTARY MATERIAL

The Supplementary Material for this article can be found online at: https://www.frontiersin.org/articles/10.3389/fenrg.2021.765612/full#supplementary-material

REFERENCES

Bajestani, M. B., Moheb, A., and Masigol, M. (2019). Simultaneous Optimization of Adsorption Capacity and Stability of Hydrothermally Synthesized Spinel Ion Sieve Composite Adsorbents for Selective Removal of Lithium from Aqueous Solutions. *Ind. Eng. Chem. Res.* 58 (27), 12207–12215. doi:10.1021/acs.iecr.9b00804

Chen, J., Lin, S., and Yu, J. (2020). Quantitative Effects of Fe_3O_4 Nanoparticle Content on Li+ Adsorption and Magnetic Recovery Performances of Magnetic Lithium-Aluminum Layered Double Hydroxides in Ultrahigh Mg/Li Ratio Brines. *J. Hazard. Mater.* 388, 122101. doi:10.1016/j.jhazmat.2020.122101

Chitrakar, R., Kanoh, H., Miyai, Y., and Ooi, K. (2001). Recovery of Lithium from Seawater Using Manganese Oxide Adsorbent ($H_{1.6}Mn_{1.6}O_4$) Derived from $Li_{1.6}Mn_{1.6}O_4$. *Ind. Eng. Chem. Res.* 40, 2054–2058. doi:10.1021/ie000911h

Chitrakar, R., Makita, Y., Ooi, K., and Sonoda, A. (2014). Lithium Recovery from Salt lake Brine by H_2TiO_3. *Dalton Trans.* 43, 8933–8939. doi:10.1039/c4dt00467a

Choi, H. A., Park, H. N., and Won, S. W. (2017). A Reusable Adsorbent Polyethylenimine/polyvinyl Chloride Crosslinked Fiber for Pd(II) Recovery from Acidic Solutions. *J. Environ. Manage.* 204, 200–206. doi:10.1016/j.jenvman.2017.08.047

Clara, M. T., and Martins, C. J. A. P. (2020). Primordial Nucleosynthesis with Varying Fundamental Constants. *A&A* 633 (6), L11. doi:10.1051/0004-6361/201937211

Deng, S., Wang, P., Zhang, G., and Dou, Y. (2016). Polyacrylonitrile-based Fiber Modified with Thiosemicarbazide by Microwave Irradiation and its Adsorption Behavior for Cd(II) and Pb(II). *J. Hazard. Mater.* 307 (15), 64–72. doi:10.1016/j.jhazmat.2016.01.002

Feng, Q., Miyai, Y., Kanoh, H., and Ooi, K. (1993). Lithium(1+) and Magnesium(2+) Extraction and Lithium(1+) Insertion Reactions with Lithium Magnesium Manganese Oxide ($LiMg_{0.5}Mn_{1.5}O_4$) Spinel in the Aqueous Phase. *Chem. Mater.* 5, 311–316. doi:10.1021/cm00027a013

Gao, A., Sun, Z., Li, S., Hou, X., Li, H., Wu, Q., et al. (2018). The Mechanism of Manganese Dissolution on $Li_{1.6}Mn_{1.6}O_4$ Ion Sieves with HCl. *Dalton Trans.* 47 (11), 3864–3871. doi:10.1039/c8dt00033f

Hong, H.-J., Ryu, T., Park, I.-S., Kim, M., Shin, J., Kim, B.-G., et al. (2018). Highly Porous and Surface-Expanded Spinel Hydrogen Manganese Oxide (HMO)/Al_2O_3 Composite for Effective Lithium (Li) Recovery from Seawater. *Chem. Eng. J.* 337, 455–461. doi:10.1016/j.cej.2017.12.130

Kong, H., Gao, C., and Yan, D. (2004). Functionalization of Multiwalled Carbon Nanotubes by Atom Transfer Radical Polymerization and Defunctionalization of the Products. *Macromolecules* 37 (11), 4022–4030. doi:10.1021/ma049694c

Lee, J., Kitchaev, D. A., Kwon, D.-H., Lee, C.-W., Papp, J. K., Liu, Y.-S., et al. (2018). Reversible Mn^{2+}/Mn^{4+} Double Redox in Lithium-Excess Cathode Materials. *Nature* 556, 185–190. doi:10.1038/s41586-018-0015-4

Liu, D., Zhang, Y., and Su, Z. (2020). Hydrometallurgical Regeneration of $LiMn_2O_4$ Cathode Scrap Material and its Electrochemical Properties. *ChemistrySelect* 5, 6697–6704. doi:10.1002/slct.201904792

Meshram, P., Pandey, B. D., and Mankhand, T. R. (2014). Extraction of Lithium from Primary and Secondary Sources by Pre-treatment, Leaching and Separation: A Comprehensive Review. *Hydrometallurgy* 150, 192–208. doi:10.1016/j.hydromet.2014.10.012

Moazeni, M., Hajipour, H., Askari, M., and Nusheh, M. (2015). Hydrothermal Synthesis and Characterization of Titanium Dioxide Nanotubes as Novel Lithium Adsorbents. *Mater. Res. Bull.* 61 (jan), 70–75. doi:10.1016/j.materresbull.2014.09.069

Nie, Z., Bu, L., Zheng, M., and Huang, W. (2011). Experimental Study of Natural Brine Solar Ponds in Tibet. *Solar Energy* 85 (7), 1537–1542. doi:10.1016/j.solener.2011.04.011

Qiu, Z., Wang, M., Chen, Y., Zhang, T., Yang, D., and Qiu, F. (2021). $Li_4Mn_5O_{12}$ Doped Cellulose Acetate Membrane with Low Mn Loss and High Stability for Enhancing Lithium Extraction from Seawater. *Desalination* 506, 115003. doi:10.1016/j.desal.2021.115003

Ramos-Sanchez, G., Callejas-Tovar, A., Scanlon, L. G., and Balbuena, P. B. (2013). DFT Analysis of Li Intercalation Mechanisms in the Fe-Phthalocyanine Cathode of Li-Ion Batteries. *Phys. Chem. Chem. Phys.* 16 (2), 743–752. doi:10.1039/c3cp53161a

Robinson, D. M., Go, Y. B., Greenblatt, M., and Dismukes, G. C. (2010). Water Oxidation by λ-MnO_2: Catalysis by the Cubical Mn_4O_4 Subcluster Obtained by Delithiation of Spinel $LiMn_2O_4$. *J. Am. Chem. Soc.* 132, 11467–11469. doi:10.1021/ja1055615

Romero, V. C. E., Putrino, D. S., Tagliazucchi, M., Flexer, V., and Calvo, E. J. (2020). Electrochemical Flow Reactor for Selective Extraction of Lithium Chloride from Natural Brines. *J. Electrochem. Soc.* 167 (12), 120522. doi:10.1149/1945-7111/abace8

Salih, A., Ahmad, M., Ibrahim, N., Dahlan, K., Tajau, R., Mahmood, M., et al. (2015). Synthesis of Radiation Curable Palm Oil-Based Epoxy Acrylate: NMR and FTIR Spectroscopic Investigations. *Molecules* 20 (8), 14191–14211. doi:10.3390/molecules200814191

Shi, C., Jing, Y., Xiao, J., Wang, X., and Jia, Y. (2017). Liquid-liquid Extraction of Lithium Using Novel Phosphonium Ionic Liquid as an Extractant. *Hydrometallurgy* 169, 314–320. doi:10.1016/j.hydromet.2017.02.015

Sileika, T. S., Kim, H.-D., Maniak, P., and Messersmith, P. B. (2011). Antibacterial Performance of Polydopamine-Modified Polymer Surfaces Containing Passive and Active Components. *ACS Appl. Mater. Inter.* 3 (12), 4602–4610. doi:10.1021/am200978h

Sun, Y., Guo, X., Hu, S., and Xiang, X. (2019). Highly Efficient Extraction of Lithium from Salt lake Brine by LiAl-Layered Double Hydroxides as Lithium-Ion-Selective Capturing Material. *J. Energ. Chem.* 34, 80–87. doi:10.1016/j.jechem.2018.09.022

Tarascon, J.-M. (2010). Is Lithium the New Gold? *Nat. Chem* 2 (6), 510. doi:10.1038/nchem.680

Torrejos, R. E. C., Nisola, G. M., Song, H. S., Han, J. W., Lawagon, C. P., Seo, J. G., et al. (2016). Liquid-liquid Extraction of Lithium Using Lipophilic dibenzo-14-crown-4 Ether Carboxylic Acid in Hydrophobic Room Temperature Ionic Liquid. *Hydrometallurgy* 164, 362–371. doi:10.1016/j.hydromet.2016.05.010

Wang, H., Wang, Z., Yue, R., Gao, F., Ren, R., Wei, J., et al. (2020). Functional Group-Rich Hyperbranched Magnetic Material for Simultaneous Efficient Removal of Heavy Metal Ions from Aqueous Solution. *J. Hazard. Mater.* 384, 121288. doi:10.1016/j.jhazmat.2019.121288

Wang, J., Pan, K., He, Q., and Cao, B. (2013). Polyacrylonitrile/polypyrrole Core/shell Nanofiber Mat for the Removal of Hexavalent Chromium from Aqueous Solution. *J. Hazard. Mater.* 244-245 (JAN.15), 121–129. doi:10.1016/j.jhazmat.2012.11.020

Wu, G., and Huang, M. (2006). Organolithium Reagents in Pharmaceutical Asymmetric Processes. *ChemInform* 37 (41), no. doi:10.1002/chin.200641252

Wu, J., Chen, J., Huang, Y., Feng, K., Deng, J., Huang, W., et al. (2019). Cobalt Atoms Dispersed on Hierarchical Carbon Nitride Support as the Cathode Electrocatalyst for High-Performance Lithium-Polysulfide Batteries. *Sci. Bull.* 64 (24), 1875–1880. doi:10.1016/j.scib.2019.08.016

Xiao, J.-L., Sun, S.-Y., Song, X., Li, P., and Yu, J.-G. (2015). Lithium Ion Recovery from Brine Using Granulated Polyacrylamide-MnO_2 Ion-Sieve. *Chem. Eng. J.* 279, 659–666. doi:10.1016/j.cej.2015.05.075

Xiao, J., Nie, X., Sun, S., Song, X., Li, P., and Yu, J. (2015). Lithium Ion Adsorption-Desorption Properties on Spinel $Li_4Mn_5O_{12}$ and pH-dependent Ion-Exchange Model. *Adv. Powder Technol.* 26, 589–594. doi:10.1016/j.apt.2015.01.008

Xu, X., Chen, Y., Wan, P., Gasem, K., Wang, K., He, T., et al. (2016). Extraction of Lithium with Functionalized Lithium Ion-Sieves. *Prog. Mater. Sci.* 84, 276–313. doi:10.1016/j.pmatsci.2016.09.004

Xu, X., Hu, W., Liu, W., Wang, D., Huang, Q., and Chen, Z. (2021). Study on the Economic Benefits of Retired Electric Vehicle Batteries Participating in the Electricity Markets. *J. Clean. Prod.* 286, 125414. doi:10.1016/j.jclepro.2020.125414

Yu, X., Zheng, M., Zeng, Y., and Wang, L. (2019). Solid-Liquid Equilibrium of Quinary Aqueous Solution Composed of Lithium, Potassium, Rubidium, Magnesium, and Borate at 323.15 K. *J. Chem. Eng. Data* 64 (12), 5681–5687. doi:10.1021/acs.jced.9b00700

Zhang, Y., Lv, W., Huang, Z., Zhou, G., Deng, Y., Zhang, J., et al. (2019). An Air-Stable and waterproof Lithium Metal Anode Enabled by Wax Composite Packaging. *Sci. Bull.* 64 (013), 910–917. doi:10.1016/j.scib.2019.05.025

Zhong, J., Lin, S., and Yu, J. (2021). Lithium Recovery from Ultrahigh Mg^{2+}/Li^+ Ratio Brine Using a Novel Granulated Li/Al-LDHs Adsorbent. *Separat. Purif. Technol.* 256, 117780. doi:10.1016/j.seppur.2020.117780

Zhu, S., Asim Khan, M., Wang, F., Bano, Z., and Xia, M. (2020). Rapid Removal of Toxic Metals Cu^{2+} and Pb^{2+} by Amino Trimethylene Phosphonic Acid Intercalated Layered Double Hydroxide: A Combined Experimental and DFT Study. *Chem. Eng. J.* 392, 123711. doi:10.1016/j.cej.2019.123711

Conflict of Interest: The authors declare that the research was conducted in the absence of any commercial or financial relationships that could be construed as a potential conflict of interest.

Publisher's Note: All claims expressed in this article are solely those of the authors and do not necessarily represent those of their affiliated organizations, or those of the publisher, the editors and the reviewers. Any product that may be evaluated in this article, or claim that may be made by its manufacturer, is not guaranteed or endorsed by the publisher.